

# Decade-long shift in the rate of global mean sea-level rise

**Hyeonsoo Cha**

Jeju National University

**Jae-Hong Moon** (✉ [jhmoon@jejunu.ac.kr](mailto:jhmoon@jejunu.ac.kr))

Jeju National University

**Taekyun Kim**

Jeju National University

**Yuhe Tony Song**

Jet Propulsion Laboratory

---

## Article

**Keywords:** global mean sea level (GMSL), ocean heat-content estimates, satellite measurements

**Posted Date:** February 3rd, 2021

**DOI:** <https://doi.org/10.21203/rs.3.rs-138706/v1>

**License:** © ⓘ This work is licensed under a Creative Commons Attribution 4.0 International License.

[Read Full License](#)

---

## **Decade-long shift in the rate of global mean sea-level rise**

### **Summary**

**Recent advances in satellite measurements and ocean heat-content estimates have enabled the monitoring of global mean sea level (GMSL) budget components and understanding of ocean effects on the Earth's energy imbalance and hydrology. We observed a notable accelerating GMSL rise rate in the recent decade after the warming "hiatus" during the 2000s, and demonstrated that this was attributed to decade-long shifts in ocean heat storage and hydrology. Since ~2011, climate-driven changes have resulted in additional ocean mass gain ( $271\pm 89$  Gt yr<sup>-1</sup>) from glacier-free land water storage and increased ocean heat uptake ( $0.28\pm 0.17$  W m<sup>-2</sup>), accelerating the GMSL rise rate by  $1.4\pm 0.4$  mm yr<sup>-1</sup>. The suggested estimates of sea-level and Earth's energy budgets highlight the importance of natural variability in understanding the impacts of the ongoing sea-level rise.**

## Introduction

Globally, the sea level has increased by more than 20 cm over the past century, and has been rising by nearly 3 mm yr<sup>-1</sup> during the past two decades<sup>1,2</sup>. An apparent increasing rate of the global mean sea level (GMSL) in the second decade of the altimetry era, i.e. during the 2000s, has been reported, and has been primarily attributed to the increasing ice mass loss in Greenland<sup>3,4</sup>. This accelerated GMSL rise contrasts with the conclusions of previous works that indicate a slowdown of this rate during the 2000s, which was attributed to the climate-driven water mass exchange between ocean and land<sup>5-7</sup>. This decade-long decrease in GMSL rate coincides with the pause in the global mean surface temperature warming, commonly known as the recent hiatus<sup>8-10</sup>. Furthermore, this decade-long surface warming hiatus has been one of the most debated and researched issues in recent years. During the hiatus period, the global ocean has been suggested to absorb extra heat because of anthropogenic radiative forcing<sup>11-13</sup>. However, more recent analyses and observations have revealed that the ocean heat uptake tended to slow down during the warming hiatus in the 2000s compared to the recent decade after 2011<sup>14,15</sup>.

These disagreements may be linked to natural climate variability, which masks the background trend of the observed sea level and, consequently, changes the acceleration values over short time scales<sup>16,17</sup>. Because the ocean stores over 90% of the Earth's energy imbalance (EEI) in the form of ocean heat content (OHC) and reflects changes in water storage between

the land and ocean, natural changes in OHC and exchange of water mass significantly affect the rate of GMSL rise. Therefore, estimating climate-driven sea-level variations is essential to improve our understanding of global ocean responses to the Earth's climate system. In addition, understanding the GMSL response to natural fluctuations can provide a more accurate background to predict sea-level changes in the future.

Despite the significance of determining GMSL and its changes, the following aspects still remain unclear: (i) how natural variability has shifted the rate of GMSL during and after the surface warming hiatus, (ii) whether the sea-level shift will persist or pause in the near future, and (iii) what are the relative steric and barystatic contributions to changes in the GMSL rate, and their relationship to EEI at the top of atmosphere (TOA)<sup>15,18–20</sup>. Herein, these issues are discussed considering the influence of the Earth's energy storage and global hydrological cycle in the closure of the sea-level budget, and in order to distinguish an intrinsic GMSL trend from naturally occurring variability.

### **Decade-long shift in GMSL**

We assessed the sea-level budget in terms of different contributions, using a number of available datasets for altimetry-based sea levels and steric and mass components (Fig. 1a). Ensemble means were applied for all terms of the sea-level budget, with a correction of TOPEX-A instrumental drift for the altimeter datasets<sup>4,21</sup>. The temporal evolution of altimetric

GMSL agrees well with the sum of all components (Fig. 1a, upper), and the linear trend difference between the two GMSLs is small ( $0.01 \text{ mm yr}^{-1}$ ), indicating the closure of GMSL budget and consistency of different datasets. These records show sea-level fluctuations superimposed on the dominant background trend with small but significant decade-long shift in the GMSL rise. The shifting trend occurred since  $\sim 2011$ , with a notable accelerating rate of GMSL rise, which coincides with a recent resumption of global mean surface temperature<sup>22</sup> (GMST) warming after the decade-long hiatus<sup>23</sup> (Fig. 1a, bottom). To diagnose the rate of GMSL rise over recent decades, we used an ensemble empirical mode decomposition (EEMD) method<sup>24</sup>, which has been widely used for many geophysical applications<sup>3,25–28</sup>. EEMD is an adaptive and temporally local decomposition method that can separate a dataset into a finite number of intrinsic mode functions that represent the non-stationary nature of climate data and residuals (Materials and Methods). Throughout the altimeter era, a distinct decade-long shift was identified in both the ensemble mean GMSL and sum of all components (Fig. 1b, upper), which are in phase with a downward shift during the global warming hiatus in the 2000s and subsequently, in phase with an upward shift (Fig. 1b, bottom). Without a secular trend, the rates of sea-level rise display a transition trend from positive to negative during the surface warming slowdown; however, the trend transitioned back to positive in 2011. The contribution to the decadal shift in the rate of GMSL rise was mostly derived from the steric expansion due to ocean warming and land water storage (LWS) excluding glaciers and ice sheets, with little

contribution from other components. For the altimeter period, the contributions of steric and LWS accounted for 71% and 69%, respectively, of the variance in the sum of all components of the GMSL budget, similar to the contributions obtained by Hamlington<sup>20</sup>. The LWS contribution estimated here strongly supports the conclusion of Reager<sup>6</sup>, who showed that glacier-free LWS slowed the rate of GMSL rise in 2002–2014. Our analysis indicates that both steric and LWS components suppressed the GMSL rise during the recent warming slowdown, despite water losses from the ice sheets. However, these two contributors significantly affected the increase in the background trend of GMSL after the end of the hiatus.

### **Climate-driven Land Water Storage**

To investigate the response of global hydrology and ocean heat storage to climate decadal variability, the following two decadal periods were compared: 2002–2010 (i.e. hiatus period) and 2011–2017. Prior to the Gravity Recovery and Climate Experiment (GRACE) record that extends back to only 2002, global hydrological models estimated the trend and fluctuation of total LWS. However, there were still uncertainties regarding the model’s ability to reproduce the interannual to decadal variability in global LWS<sup>29</sup>. Moreover, the large uncertainty in the OHC calculation that arises from insufficient sampling and instrumental biases was mainly observed for the period before the early 2000s, that is, the pre-Argo period<sup>30,31</sup>. Therefore, we used the GRACE and Argo-based products to estimate the global patterns of decadal trends in

the LWS and OHC for the two analysis periods. The global estimate of GRACE trend over 2002–2010 revealed an increasing LWS (wetting) at low latitudes, and decreasing LWS (drying) at the mid-latitude of the southern hemisphere (Fig. 2), consistent with previous GRACE studies<sup>6,32</sup>. These latitudinal trends in LWS shifted since 2011, showing a distinct pattern of mid-latitude wetting and low latitude drying, which is more pronounced in the southern hemisphere. The decadal trend shift resulted from changes in the LWS regime since 2011, from wet to dry conditions at low latitudes, and from dry to wet conditions at mid-latitudes. For instance, the strongest negative trends at low latitudes over the recent decade were attributed to major droughts across the Amazon basin and parts of southern Africa and Australia in 2015–2016<sup>33,34</sup>. The spatial patterns of the LWS trend strongly resembled the LWS pattern regressed on the EEMD-determined decadal mode of the Pacific Decadal Oscillation (PDO; Fig. 3a)<sup>35,36</sup>, thereby implying an important decadal persistence in the Earth’s climate systems<sup>7</sup>. The GRACE-derived LWS was consistent with the observed land precipitation from the Global Precipitation Climatology Project (GPCP) in the decadal trends and in its interannual variations throughout the GRACE period (Fig. 2). When land precipitation was converted into LWS through water distribution in soils and aquifers, there was a delayed (7–10 months) response of LWS to the precipitation in land, supporting the findings of Zhang<sup>37</sup>.

The glacier-free LWS contributed  $0.14 \pm 0.11$  and  $1.04 \pm 0.21$  mm yr<sup>-1</sup> to the GMSL during the first and second decades of the GRACE period, respectively (Fig. 4). Because the net LWS

changes estimated here include human- and climate-driven components in storage, an Intergovernmental Panel on Climate Change (IPCC) estimate<sup>1</sup> of direct human-induced LWS changes ( $0.38 \pm 0.12 \text{ mm yr}^{-1}$ ) was used to calculate the climate-driven LWS contribution to GMSL, similar to the approach used in Reager<sup>6</sup>. Therefore, the climate-driven LWS suppressed the GMSL rise ( $-0.23 \pm 0.16 \text{ mm yr}^{-1}$ ) over the hiatus period but subsequently enhanced it ( $0.66 \pm 0.24 \text{ mm yr}^{-1}$ ), which suggests that the natural LWS variability significantly contributed to the decade-long shift in the GMSL. These LWS changes determined by GRACE indicate that naturally occurring variability in precipitation leads to decadal changes in the exchange of water between land and ocean.

### **Ocean effect on the Earth Energy Imbalance**

The steric contribution to GMSL rise arises from changes in OHC, which is the major factor sequestering the EEI resulting from rising CO<sub>2</sub> concentrations. To elucidate OHC fluctuations contributing to the rate of GMSL rise, we analysed the temperature profiles recorded by Argo array floats since 2005, which provided a reliable OHC estimate over 0–2000 m<sup>30,38</sup>. Global maps of OHC (derived from the Scripps Institution of Oceanography (SCRIPPS) product) trends over the two decadal periods revealed that since 2011, the trend has been shifting toward an opposite pattern compared to that of the preceding period (Fig. 5). It is evident from the regression pattern of the EEMD-determined decadal mode of the PDO that

there are global oceanic responses to Pacific climate variability (Fig. 3b), consistent with the linear trend maps of the OHC. In 2005–2010, the OHC showed strong warming trends in the western tropical Pacific and eastern/southeastern Indian, and a warming structure centred in the western/central North Pacific, which is surrounded by cooling along the Pacific coast of North America. With the PDO transitioning back to positive since 2011, the spatial patterns of the OHC trend were reversed, accompanied by a warming trend in the eastern Pacific and a cooling trend in the western tropical Pacific and northern and southeastern Indian<sup>9,28</sup>. The trend reversal was also observed in the North Atlantic, with cooling in the subpolar gyre and warming in the subtropical gyre, which indicates a significant influence of ocean circulation on heat redistribution. It is worth noting that the decadal OHC trend in the North Atlantic subpolar gyre might be contributing to the shifts in the melting rate of Greenland Ice Sheet (GIS). For instance, the cooling in the subpolar gyre since 2011 may have contributed to slow down of the rate of ice loss in the GIS, which is consistent with the findings of a recent study<sup>39</sup> that identified a persistent increase in ice loss rate prior to 2012, followed by a full reversal. The combined impacts of warming and cooling regions in the OHC resulted in a GMSL fluctuation that can be largely attributed to decadal-scale climate variability.

The globally integrated OHC time series computed from the surface to a 2000 m depth based on the three Argo products is shown in Fig. 5c. Despite some spread around the mean between the three Argo products, all datasets show an increase of global OHC since 2005,

which demonstrate that the estimates of ocean warming are robust. The time series of annual global OHC after removing the trend of the whole Argo period revealed a trend shift around 2011, from a cooling to a warming trend (Fig. 5d), thereby emphasising that the trend reversal is the dominant mode of OHC change at least over the recent decades. To directly compare OHC with the satellite-observed Earth's energy storage, time-integrated TOA net flux estimated from the Clouds and the Earth's Radiant Energy System (CERES) measurement was used, and the Argo-based OHC tracked the phase of the TOA net energy storage reasonably well. Yearly variations of global OHC and CERES TOA net energy storage were correlated at 0.53, which is in good agreement with the results of previous works<sup>40-42</sup>.

To illustrate the OHC contribution to the Earth's energy budget, we estimated the EEI during and after the warming hiatus in terms of the heating rate applied over the Earth's surface area by combining Argo-observed upper-2000 m OHC with previously published estimates of heat uptake by the deeper ocean and non-ocean terms (Fig. 6). Considering a constant heating rate of  $0.136 \pm 0.087 \text{ W m}^{-2}$  at ocean depths below those sampled by Argo floats<sup>43</sup>, as well as the sum of non-ocean terms<sup>44</sup> of  $0.071 \text{ W m}^{-2}$ , we obtained a net heat uptake of  $0.57 \pm 0.13$  and  $0.86 \pm 0.12 \text{ W m}^{-2}$  for 2005–2010 and 2011–2017, respectively. The comparison between the two periods indicates that the global ocean gained more heat energy from 2011 onwards ( $0.28 \pm 0.17 \text{ W m}^{-2}$ ), as compared with the previous period. The EEI estimated from the latest release of CERES satellite data was  $0.60 \pm 0.10 \text{ W m}^{-2}$  for 2005–2010 and  $0.95 \pm 0.10 \text{ W m}^{-2}$  for

2011–2017, which indicates a close correspondence between two completely independent EEI estimates on decadal time scales. The two EEI estimates are not distinguishable within the estimated uncertainty and thus, the increase in the ocean heat uptake since 2011 seems to be robust. Fig. 6 further demonstrates the agreement with the EEI obtained from the altimetry minus GRACE residual approach<sup>45,46</sup>. These results strengthen confidence in all three complementary climate observing systems<sup>47</sup>. Furthermore, the consistency shown here suggests that there was no shortfall in closing the global energy budget during the 2000s, in contrast to the so-called “missing energy” problem<sup>48</sup>.

## Summary

The resulting relationship between sea-level rise, precipitation, ocean warming, and TOA net flux demonstrates a physically consistent expression of decadal climate variability on global scales. Our results can further clarify the ocean’s role in EEI and hydrological cycle and perspectives on ongoing sea-level change. An ongoing GMSL rise can be influenced by climate-driven signals that can accelerate or decelerate the underlying sea-level trend for decadal time periods. Furthermore, the estimate conducted here illustrates the utility of completely independent datasets for EEI cross validation by emphasising the consistency of thermal energy in the Earth system. Although systematic errors of space observations and in situ uncertainties are likely to remain large owing to unsampled regions and/or mapping choice,

efforts to extend both satellite measurements and Argo records with ongoing development of Deep Argo floats<sup>49</sup> will allow better monitoring of EEI changes and provide accurate datasets to investigate the ocean's role in the Earth's energy budget and future sea-level rise<sup>40</sup>.

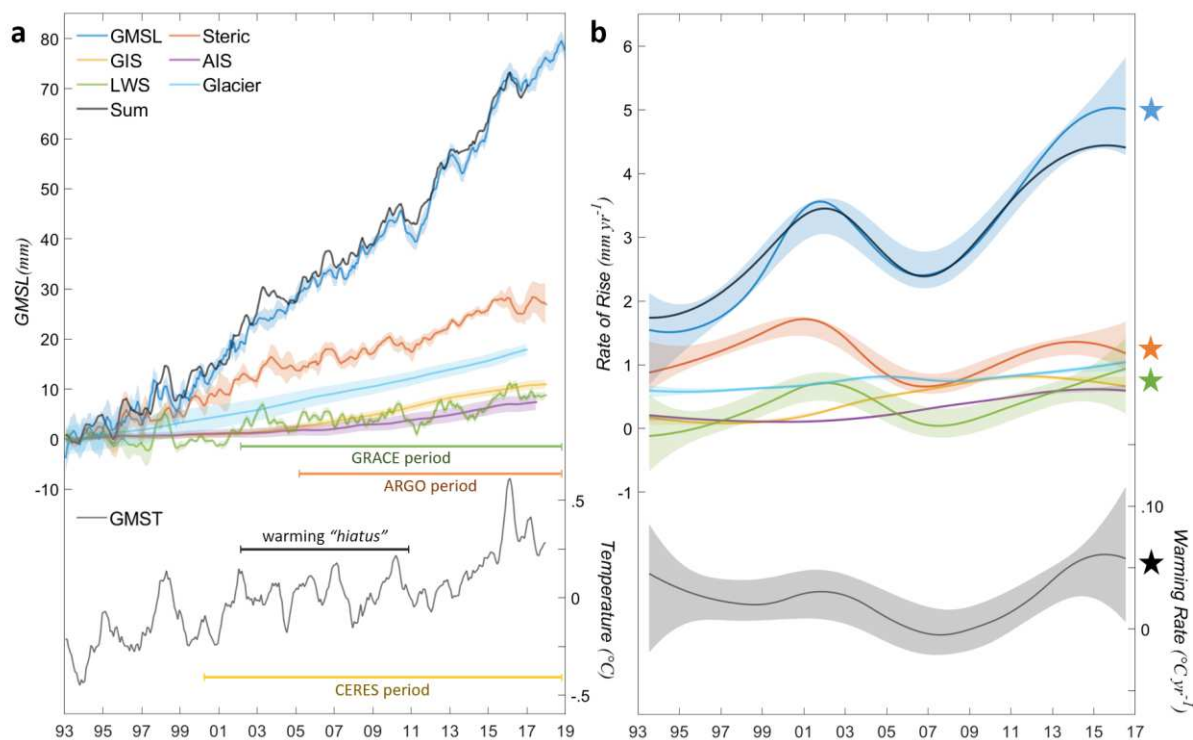


**Fig. 1. | GMSL budget and GMST. (a)** Time series of all sea-level components (upper) and GMST (bottom), including the ensemble mean GMSL using altimetry data from six processing groups (blue, see Materials and Methods), sum of ensemble mean components (black), individual ensemble mean components, and GMST using the Goddard Institute for Space Studies Surface Temperature Analysis v4<sup>22</sup>. Uncertainties are based on the dispersion among different time series around the mean (coloured shades). **(b)** Instantaneous rate of GMSL trend with decadal variability (upper) and GMST trend (bottom) from EEMD analysis. A bootstrap method based on random resampling to estimate confidence intervals (coloured shades) was used to test the significance (see Materials and Methods). Time series with decadal shift are highlighted (star symbols).

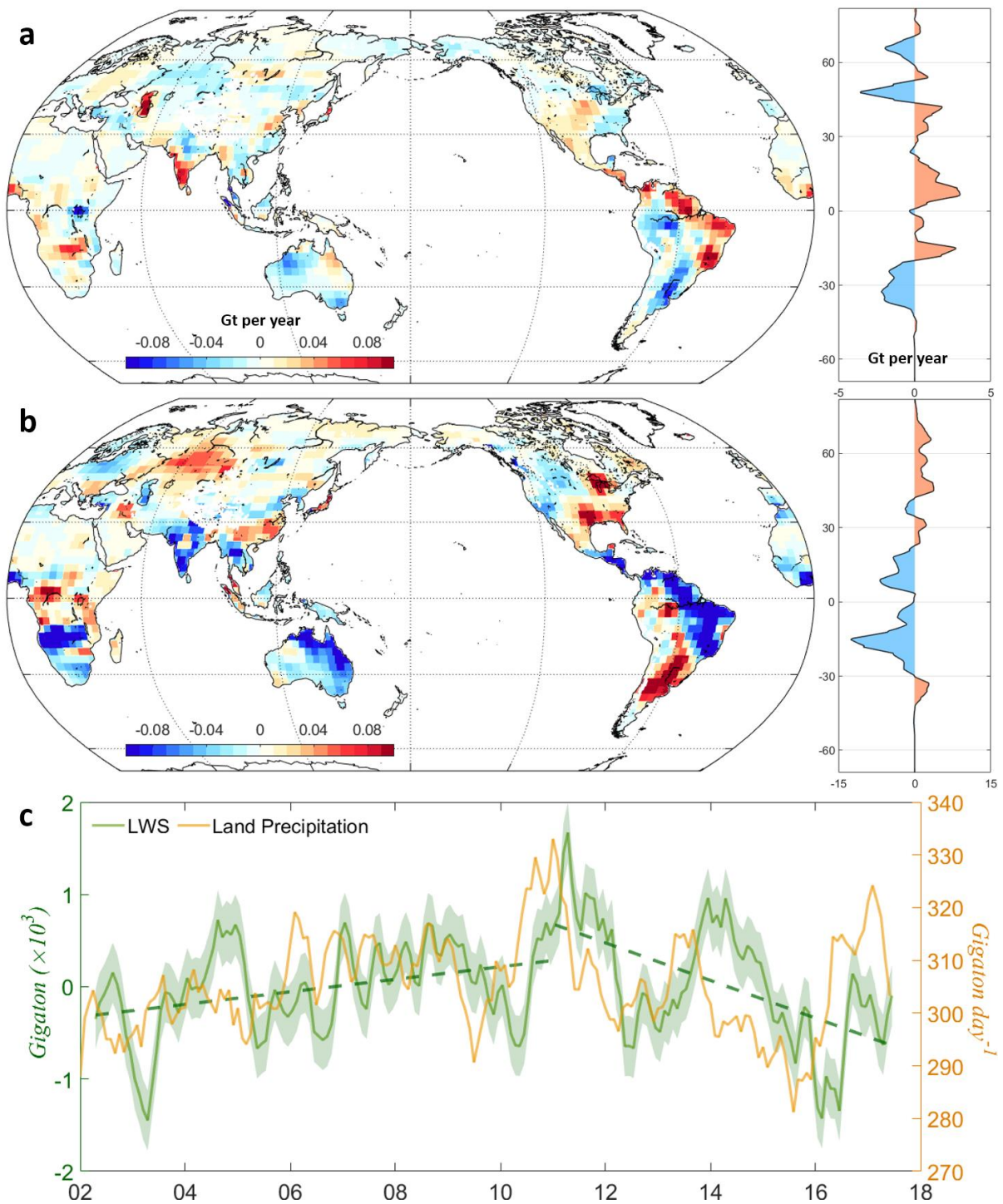


**Fig. 2. | Trends in LWS from GRACE observations.** Global map of LWS trend and its zonal total trend in (a) in 2002–2010 and (b) 2011–2017. (c) Time series of global LWS

(green) from GRACE and land precipitation (yellow) from GPCP. The linear trend throughout the GRACE period was removed to highlight climate-driven decadal trend shift in LWS. The dashed lines indicate the linear trends in 2002–2010 and 2011–2017. The LWS uncertainties are shown in coloured shades (see Materials and Methods).

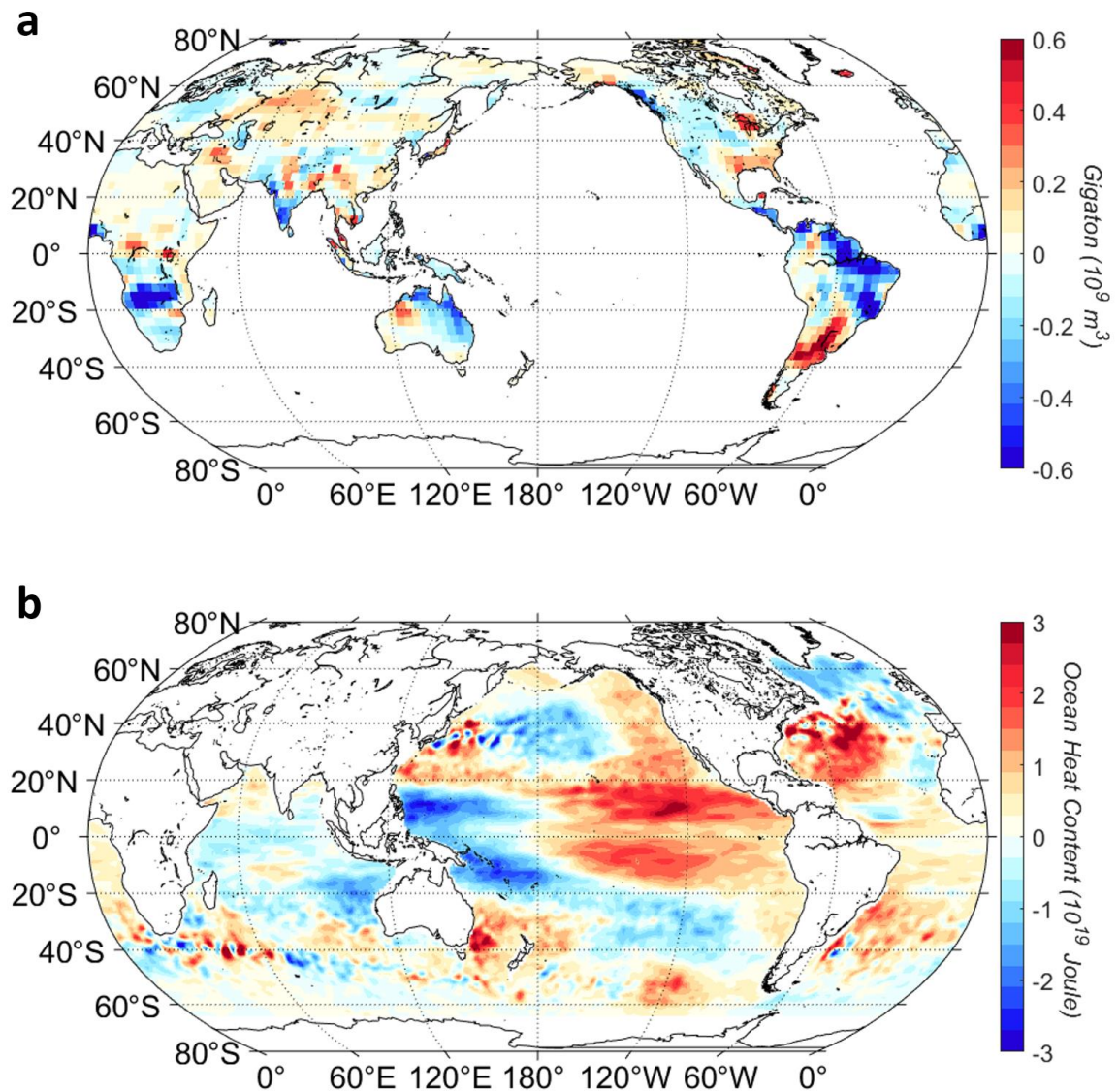


**Fig. 3 | Global LWS and OHC fingerprints with respect to the PDO. (a, b) LWS and OHC (0-2000 m) regressed onto the decadal mode of the PDO (shown in Supplementary Fig. 5c) over 2002–2017 and 2005–2017, respectively. Data sources are GRACE mascon solution (JPL RL06Mv2) for LWS and SCRIPPS for OHC, respectively.**

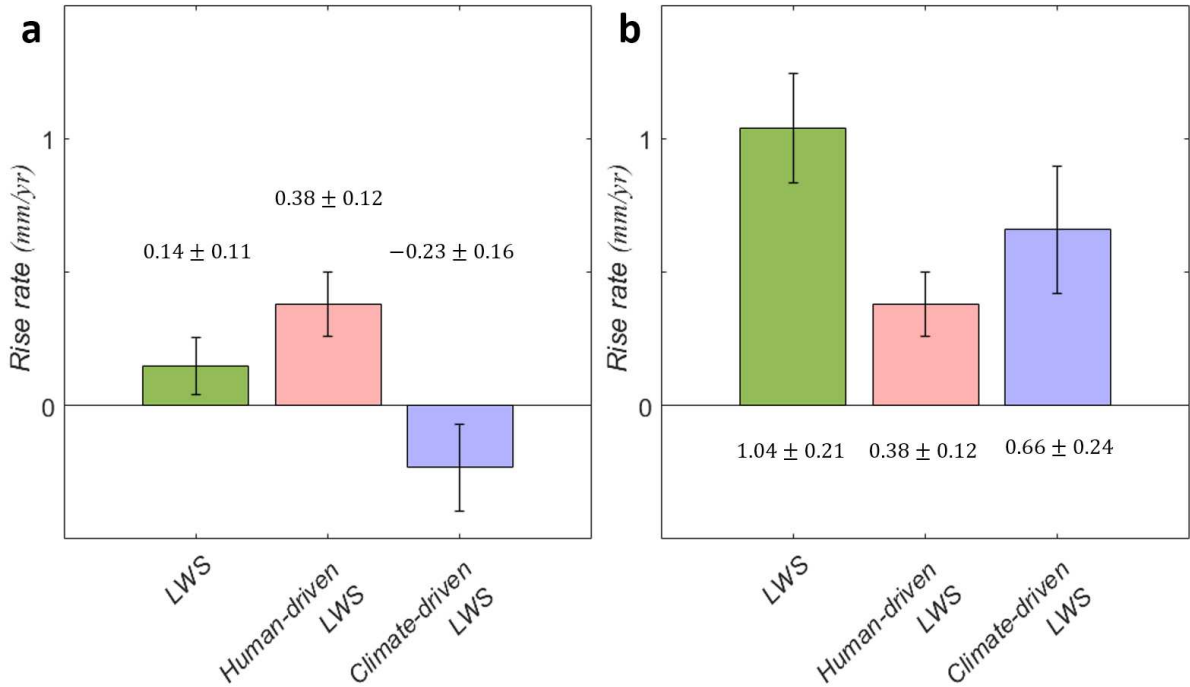


**Fig. 4 | Disaggregation of net LWS terms. (a) 2002–2010. (b) 2011–2017.** Left bar: Glacier-free LWS, middle bar: human-driven LWS estimated by IPCC AR 5<sup>1</sup>, and right bar: Climate-driven LWS (i.e. subtracting the IPCC estimate for human-driven change). Error bars represent 95% confidence intervals estimated from slope of uncertainty and the quadratic sum.

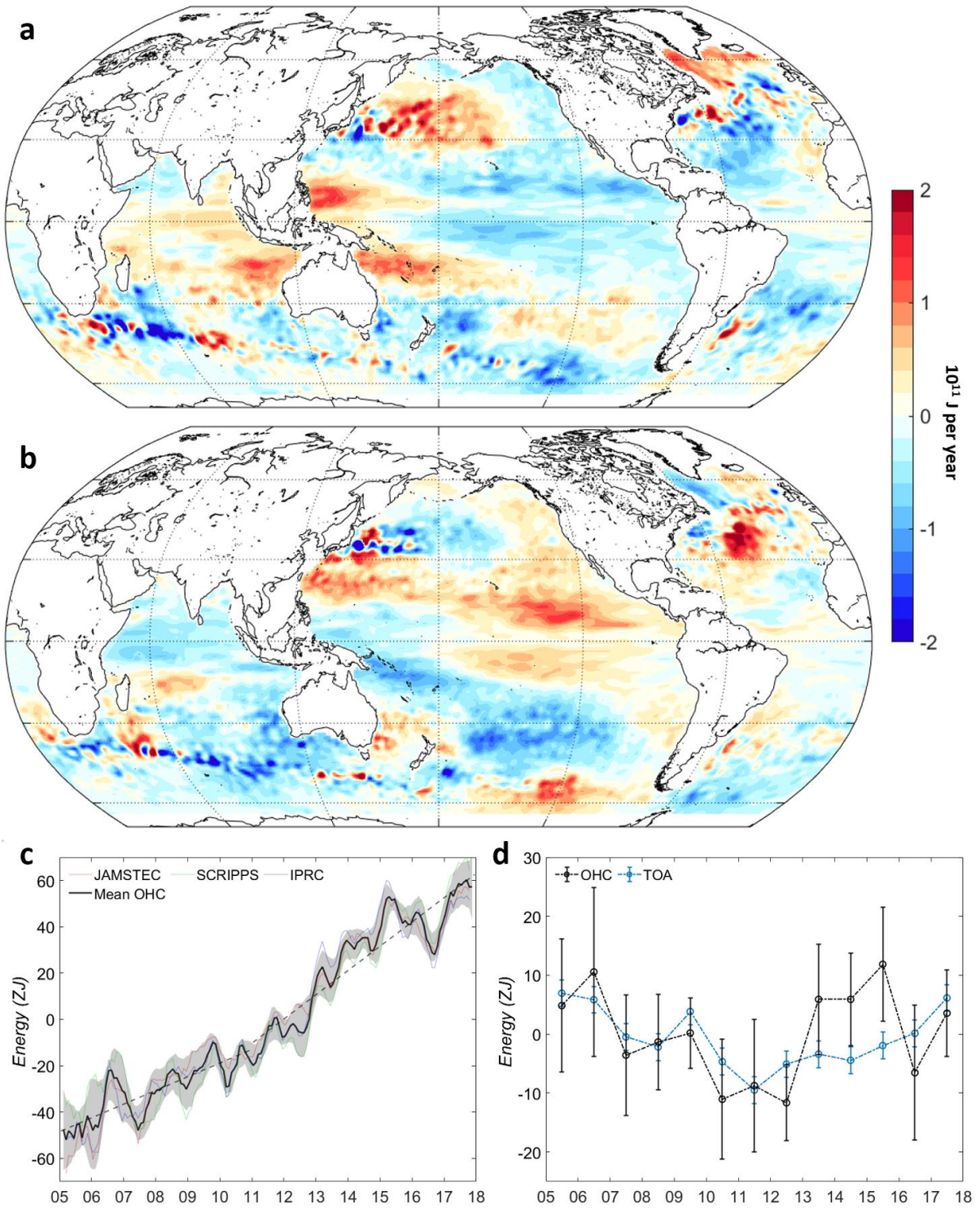


**Fig. 5. | Argo-derived OHC trends and TOA net energy storage.** Global map of upper-2000 m OHC trend from the SCRIPPS data during (a) 2005–2010 and (b) 2011–2017. (c)

Ensemble mean of globally integrated OHC (black) based on three Argo products (see Materials and Methods) and their individual values (coloured lines). The shaded areas denote one standard deviation around the mean. **(d)** Comparison between the yearly OHC (black) and TOA net energy storage (blue). Each component was detrended for the study period. The OHC uncertainties (black bar) are shown at one standard error of the mean, and TOA annual random errors (blue bar) are based on Johnson<sup>41</sup>.

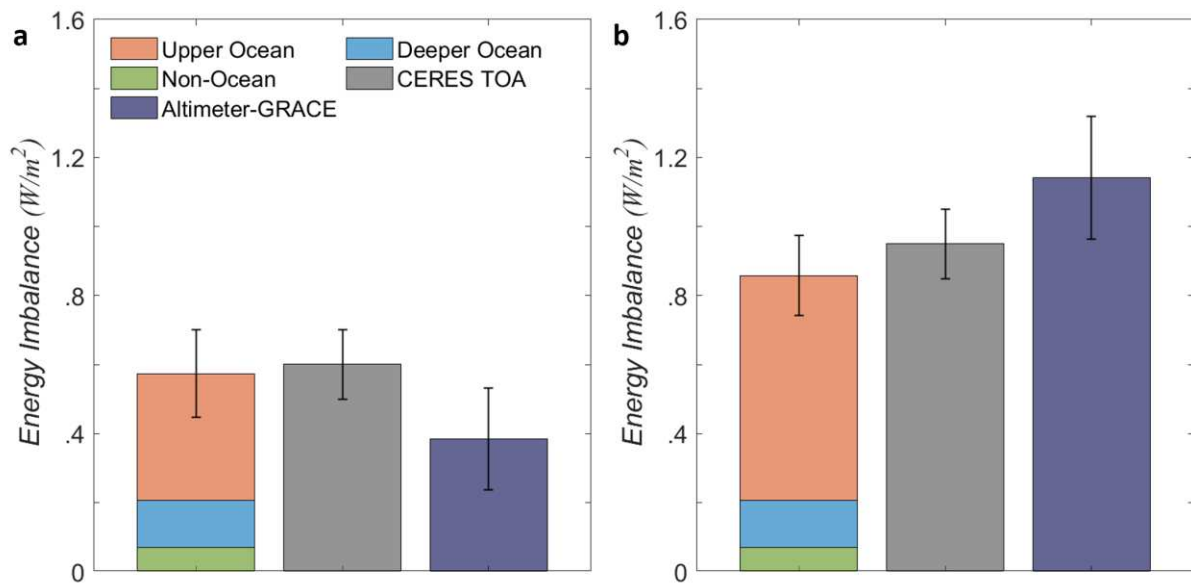


**Fig. 6. | Three independent estimated contribution to EEI. (a) 2005–2010. (b) 2011–2017.**

Left bar: in situ observational estimate of ocean heat uptake by combining Argo-based upper ocean (0–2000 m) and previously published estimates of heat uptake by the deeper ocean terms<sup>42</sup> and non-ocean term<sup>43</sup>; middle: direct CERES satellite measurements of TOA net energy flux, and right: altimetry minus GRACE residual approach. Error bars represent 95% confidence intervals estimated from slopes of uncertainty fitted to each data. Uncertainties of CERES TOA flux are shown at one standard deviation ( $0.1 \text{ W m}^{-2}$ ) based on Johnson<sup>41</sup>.

## Methods

**Satellite altimetry.** We use six different altimetry products processed by five groups: Archiving, Validation and Interpretation of Satellite Oceanographic data (AVISO; <https://www.aviso.altimetry.fr/data/products/ocean-indicators-products/mean-sea-level.html>); Commonwealth Scientific and Industrial Research Organization (CSIRO; <https://research.csiro.au/slrwavescoast/sea-level/measurements-and-data/sea-level-data/>); Colorado University (CU 2018 Release 1; <http://sealevel.colorado.edu/content/2018rel1-global-mean-sea-level-time-series-seasonal-signals-removed>); National Oceanographic and Atmospheric Administration (NOAA; [https://www.star.nesdis.noaa.gov/socd/lisa/SeaLevelRise/LSA\\_SLR\\_timeseries.php](https://www.star.nesdis.noaa.gov/socd/lisa/SeaLevelRise/LSA_SLR_timeseries.php)); NASA, Goddard Space Flight Center (NASA-GSFC version 4; [https://podaac.jpl.nasa.gov/dataset/MERGED\\_TP\\_J1\\_OSTM\\_OST\\_GMSL\\_ASCII\\_V4](https://podaac.jpl.nasa.gov/dataset/MERGED_TP_J1_OSTM_OST_GMSL_ASCII_V4)); The Climate Change Initiative (CCI version 2; <http://www.esa-sealevel-cci.org/products>). The effect of Glacier Isostatic Adjustment (GIA) is accounted for in each GMSL time-series except for the NOAA data. The NOAA sea level data was corrected for GIA effect by using  $-0.3 \text{ mm yr}^{-1}$  based on ref.<sup>50</sup>. In addition, a correction of TOPEX-A instrumental drift for the altimeter data sets is considered ( $1.5 \text{ mm yr}^{-1}$ ) over the period of 1993–1999, except for the NASA-GSFC data, which was already corrected for the drift correction<sup>4,21,51</sup>. Similar to previous

studies<sup>3,4</sup>, we use the ensemble average from all products instead of relying on a single altimetry-derived GMSL time series. Uncertainties are based on the dispersion among different time series around the mean. Supplementary Fig. 1a shows the time-series of GMSL in each product and their ensemble average from 1993 to 2018. Detailed information of each data set is available in the corresponding website.

**Steric sea levels.** To quantify the steric component of GMSL, we use the following different data sets: Ishii and Kimoto<sup>52</sup> (hereafter IK) data set (<https://rda.ucar.edu/datasets/ds285.3/>); NOAA data set<sup>44</sup> ([https://www.nodc.noaa.gov/OC5/3M\\_HEAT\\_CONTENT/tsl\\_global.html](https://www.nodc.noaa.gov/OC5/3M_HEAT_CONTENT/tsl_global.html)); EN4 data set<sup>53</sup> (<https://www.metoffice.gov.uk/hadobs/en4/download-en4-2-0.html>). These products integrate the temperature and salinity data from the surface to 700 m depth at monthly intervals. Two of the time series cover the period of 1993–2017, but the IK data ends in 2012. Total steric sea-level is reconstructed from the ensemble average of the upper ocean time series, the estimate ( $0.24 \text{ mm yr}^{-1}$ ) from 700 to 2000 m based on Chambers<sup>54</sup> and the deep ocean trend ( $0.11 \text{ mm yr}^{-1}$ ) based on Purkey and Johnson<sup>43</sup>. After 2005, we utilize three different Argo data sets, providing temperature and salinity down to 2000 m depth at monthly intervals: The International Pacific Research Center (IPRC, [http://apdrc.soest.hawaii.edu/projects/Argo/data/gridded/On\\_standard\\_levels/index-1.html](http://apdrc.soest.hawaii.edu/projects/Argo/data/gridded/On_standard_levels/index-1.html)); The Japan Agency for Marine-Earth Science and Technology (JAMSTEC,

[https://pubargo.jamstec.go.jp/public/MOAA\\_GPV/Glb\\_PRS/OI/](https://pubargo.jamstec.go.jp/public/MOAA_GPV/Glb_PRS/OI/)); The SCRIPPS Institution of Oceanography (SCRIPPS; [http://sio-argo.ucsd.edu/RG\\_Climatology.html](http://sio-argo.ucsd.edu/RG_Climatology.html)). For the three data sets, we computed steric sea level time series from the surface down to 2000 m on a  $1^\circ \times 1^\circ$  grid for the period of January 2005 to December 2017. The estimate for the deep ocean contribution ( $0.11 \text{ mm yr}^{-1}$ ) based on Purkey and Johnson<sup>43</sup> was also added over the whole data length. During the Argo period, we use the ensemble average of all steric sea level products. The standard deviation of the residuals of the individual time series with the ensemble mean represents the systematic uncertainty. The monthly time series of steric sea level in each product and their ensemble mean are shown in Supplementary Fig. 1b.

For the period of 2005–2010, the mean rate of steric sea-level rise estimated from three Argo measurements (i.e., SCRIPPS, IPRC, JAMSTEC) is  $0.68 \pm 0.23 \text{ mm yr}^{-1}$ , whereas it becomes about two times faster ( $1.19 \pm 0.20 \text{ mm yr}^{-1}$ ) after 2011 (Supplementary Fig. 2). Previous study have found sea level rise based on thermal expansion trend using upper-1500 m Argo data of  $0.75 \pm 0.15 \text{ mm yr}^{-1}$  over 2005–2010 period<sup>55</sup>, which is comparable to our estimate within the uncertainties.

**Antarctica and Greenland Ice Sheets.** Greenland and Antarctica Ice Sheet data from the Ice sheet Mass Balance Inter-comparison Exercise (IMBIE; <http://imbie.org/data-downloads/>) are used in this study. The IMBIE data provides a reconciled estimate of ice sheet mass balance by

using satellite altimetry, space gravimetry and the input-output method<sup>56</sup>. The IMBIE supports the Antarctica ice sheet (AIS) data from January 1992 to June 2017 and newly released Greenland ice sheet (GIS) data from January 1992 to December 2018<sup>39</sup>. Uncertainty of cumulative ice sheet mass change is estimated as the root sum square of annual errors<sup>39</sup>. Supplementary Fig. 1c provides the contributions of Greenland and Antarctica ice sheets to GMSL rise and their uncertainties.

**Glaciers.** For the global glacier mass balance, we considered four time series that have different time periods: (1) Zemp<sup>57</sup> for the period 1961–2016; (2) Marzeion<sup>58</sup> for the period 1902–2013; (3) Leclercq<sup>59</sup> for the period 1800–2010, (4) Cogley<sup>60</sup> for the period 1950–2015. Because these datasets are given at annual or pentadal intervals, time series are interpolated onto regular monthly interval over 1993–2016 and we use the ensemble average across the interpolated records. We computed the uncertainty associated with each time series ( $\sigma_i$ ) and the spread around the ensemble mean ( $\sigma_{spread}$ ) through the quadratic sum:  $\sqrt{\sigma_i^2 + \sigma_{spread}^2}$ . The monthly time series of the glacier in each data set and their ensemble mean are shown in Supplementary Fig. 1d.

**Land water storage (LWS).** For LWS contributions, the GRACE mascon solution (JPL RL06Mv2) from April 2002 to Jun 2016 is used in this study. Several post-processing corrections, such as geocenter motion, GIA signal and solid earth response to tectonic events,

are applied to this RL06Mv2 solution<sup>6,61,62</sup>. To isolate LWS in GRACE mascon, we removed the glacier signals from the data over land based on Wouters<sup>63</sup>. The standard error is based on noise assessment by Groh<sup>64</sup>. Prior to the GRACE period, information on the LWS component comes from reanalysis products over 1993–2002: Modern Era Retrospective-analysis for Research and Applications (MERRA)-Land<sup>65</sup> and an updated MERRA version 2 hydrology data<sup>66</sup>, freely available at GES DISC (<https://disc.gsfc.nasa.gov/>). MERRA-Land is a land-only reanalysis data that supplements the original MERRA product<sup>65</sup>. MERRA-2 uses observation-based precipitation data to derive the land surface water budget, allowing the near-surface air temperature and humidity to respond to the improved precipitation forcing<sup>66</sup>. Supplementary Fig. 1e shows the time-series of LWS in each product and their ensemble average.

**Ocean Heat Content and Earth Energy Imbalance.** The ocean is the largest solar energy collector which stores over 90% of Earth’s Energy in the form of ocean heat content (OHC). The OHC for upper 2000 m is determined using ocean temperature ( $\theta$ ) produced by three Argo products. The OHC ( $Q$ ) is given by  $Q = \rho \cdot C_p \iiint \theta \cdot dx \cdot dy \cdot dz$  where  $C_p$  is the specific heat capacity of seawater (4,000 J kg<sup>-1</sup>K<sup>-1</sup>) and  $\rho$  is the water density. The spatial patterns of OHC trends are shown in Fig. 5 (SCRIPPS product) and Supplementary Fig. 3 (JAMSTEC and IPRC products) over the following two periods: 2005–2010 and 2011–2017. The spread between the datasets might be due to choices related to quality-control, mapping strategies, and

suitable baseline climatology by the data producers<sup>67</sup>.

The time series of annual global OHC with trend removed reveals a trend shift around 2011 from a cooling to a warming trend (Fig. 5d), emphasizing that the trend reversal is the dominant mode of OHC change at least over the recent decades. The global volume-integrated OHC trend accounts for  $59 \pm 15$  ZJ decade<sup>-1</sup> (1ZJ =  $10^{21}$  J) over 2005–2010, based on the mean estimate between the Argo products. Since 2011, the global upper-2000 m ocean heat rises at a rate of  $105 \pm 13$  ZJ decade<sup>-1</sup>, and ocean gains more heat in comparison with the preceding period. The corresponding planetary heating rates are  $0.37 \pm 0.09$  W m<sup>-2</sup> over 2005–2010 and  $0.65 \pm 0.08$  W m<sup>-2</sup> over 2011–2017 (per unit of Earth's surface of  $510 \times 10^{12}$  m<sup>2</sup>), respectively.

To examine satellite-observed Earth's energy storage, the Top of Atmosphere (TOA) net energy storage anomalies are obtained by time-integrating the TOA net energy flux data from the Clouds and the Earth's Radiant Energy System (CERES) Energy Balanced and Filled (EBAF) Ed4.0 product (<https://ceres.larc.nasa.gov/data/#energy-balanced-and-filled-ebaf>).

**Ensemble Empirical Mode Decomposition (EEMD) Method.** To extract time-varying trends in all components of sea-level budget, we use an ensemble empirical mode decomposition (EEMD) method, which has been widely used in many geophysical climatology applications. The EEMD method is based on empirical mode decomposition (EMD), which is designed to separate the time series into a finite number of intrinsic mode functions (IMFs) and residual

trend that represents the long-term adaptive trend<sup>25,68</sup>. The IMFs of EEMD is obtained as an ensemble average of IMFs that were decomposed from the original time-series with the addition of Gaussian white noise by EMD. This advanced method resolves the mode mixing problem caused by intermittence signal in the original EMD. Here, we set the white noise with variance  $\sigma=0.2$  relative to the variance of the original time-series, and the number of ensemble members,  $N=500$ . Supplementary Fig. 4 shows the EEMD results for all data sets, which yielded seven IMFs and residual in ascending order from highest-frequency to lowest-frequency. Based on spectral analysis, the EEMD-derived IMFs can be grouped into four major time-scale components: IMFs 1–2 as the high-frequency components of less than a year, IMFs 3–5 as the ENSO-scales frequencies ranging from 1.5 to 7 years, IMF 6–7 as the decadal-scales component with a peak period of  $\sim 12$  years, and taking a residual as the intrinsic trend. Note that the EEMD-determined ENSO signals are clearly separated from the decadal mode and the secular trend. The intrinsic trend is the same unit as the raw time series and the rate of time-varying trend is obtained by taking the first-order time derivative of the trend, in unit of  $\text{mm y}^{-1}$  for GMSL.

Time-varying rate of the intrinsic trend of each time series, which was determined by calculating the temporal derivative of the trend (i.e., residual mode), is presented in Supplementary Fig. 5a. A bootstrap method based on random resampling to estimate confidence intervals is used to test the significance of the intrinsic trends obtained from EEMD.

It is shown that the time-varying trends in all components do not change significantly within their confidence intervals, indicating robustness of the EEMD-derived trends. The trend rate from the sum of all components of GMSL budget increased from  $2.3 \pm 0.3 \text{ mm yr}^{-1}$  in 1993 to  $3.8 \pm 0.3 \text{ mm yr}^{-1}$  in 2017. The volumetric expansion due to ocean warming occupied 53% of the sum of the contributions in 1993; however, it reduced largely to 29% of the total contributions in 2016. In contrast, the mass inflow to the ocean due to exchange of water mass between land and ocean exhibited an increasing contribution to GMSL from 47% in 1993 to 71% of the total contributions in 2016, with the largest increase coming from the contribution of the Greenland ice sheet (GIS). These trends are consistent with a previous estimate of the time-varying trends<sup>3</sup> that showed changes in relative contributions of steric and mass components. We further identify strong relationship between the decadal mode of sea-level rise and the Pacific decadal variability derived from the EEMD decomposition of the Pacific Decadal Oscillation (PDO; ref.<sup>35,36</sup>) index (Supplementary Fig. 5c, ref.<sup>8,28,69</sup>). It is thus likely that the climate-driven decadal mode strongly contributed to slowing the rate of sea-level rise during the hiatus but accelerating the trend rate after the hiatus.

**Significance of the intrinsic trend.** The significance of the intrinsic trend is tested using a standard bootstrap method<sup>70</sup>. This method is based on randomly resampling to estimate confidence intervals. The main steps in this method are as follows: 1) create artificial resampled

data ( $\varepsilon_{rand}$ ) by randomly sampling the anomaly for the original data; 2) add the artificial data to the residual ( $x^* = \varepsilon_{rand} + R$ ); 3) perform the EEMD again on the reconstructed data ( $x^*$ ) to obtain the artificial trend; 4) repeat the steps 1–3 for M times (in this study, M=1,000 iterations) and the mean artificial trend ( $\overline{R^*}$ ) can be estimated from individual bootstrap simulations,  $\overline{R^*} = \frac{1}{m} \sum_{i=1}^M R(x_i^*)$ . Supplementary Fig. 5a,b show the rates of intrinsic trends and decadal variability in each component, with a 95% confidence interval (within two standard deviations) for 1,000 randomly sampled trends and decadal modes, respectively. The time-varying trends and decadal modes in all components do not change significantly within their confidence intervals, indicating robustness of the EEMD-derived trend and decadal mode.

In addition, to test whether the decadal-scale component was affected by the ending point effect including the significant event like El Niño, similar to Cha<sup>28,71</sup>, we compared the decadal-scale components of full record length with gradually shortened records of the same datasets by removing 0–3 years of data from the end of the time series (Supplementary Fig. 6). The amplitudes of decadal-scale components from satellite altimetry, steric, and LWS show a little change, but their decadal signal persisted regardless of the impact of the El Niño event in 2015/16, indicating that the decadal-scale variability is robust in the GMSL.

## References

1. Church, J. A. et al. in *Climate Change 2013: The physical Science Basis. Contribution of Working Group I to the Fifth Assessment Report of the Intergovernmental Panel on Climate Change*, T. F. Stocker et al., Eds. (Cambridge Univ. Press, 2013)
2. Ablain, M. et al. Satellite Altimetry-Based Sea Level at Global and Regional Scales. *Surv. Geophys.* **38**, 7-31 (2017).
3. Chen, X. et al. The increasing rate of global mean sea-level rise during 1993-2014. *Nat. Clim. Change* **7**, 492-495 (2017).
4. Dieng, H. B., Cazenave, A., Meyssignac, B. & Ablain, M. New estimate of the current rate of sea level rise from a sea level budget approach. *Geophys. Res. Lett.* **44**, 3744-3751 (2017).
5. Cazenave, A. et al. The rate of sea-level rise. *Nat. Clim. Change* **4**, 358-361 (2014).
6. Reager, J. T. et al. A decade of sea level rise slowed by climate-driven hydrology. *Science* **351**, 699-703 (2016)
7. Hamlington, B. D., Reager, J. T., Lo, M.-H., Karnauskas, K. B. & Leben, R. R. Separating decadal global water cycle variability from sea level rise. *Sci. Rep.* **7**, 1-7 (2017).
8. England, M. H. et al. Recent intensification of wind-driven circulation in the Pacific and the ongoing warming hiatus. *Nat. Clim. Change* **4**, 222-227 (2014).

9. Kosaka, Y. & Xie, S. P. Recent global-warming hiatus tied to equatorial Pacific surface cooling. *Nature* **501**, 403-407 (2013).
10. Maher, N., England, M. H., Gupta, A. S. & Spence, P. Role of Pacific trade winds in driving ocean temperatures during the recent slowdown and projections under a wind trend reversal. *Clim. Dyn.* **51**, 321-336 (2018).
11. Balmaseda, M. A., Trenberth, K. E. & Kallen, E. Distinctive climate signals in reanalysis of global ocean heat content. *Geophys. Res. Lett.* **40**, 1754-1759 (2013).
12. Chen, X. & Tung, K. K. Varying planetary heat sink led to global-warming slowdown and acceleration. *Science* **345**, 897-903 (2014).
13. Trenberth, K. E., Fasullo, J. T. & Balmaseda, M. A. Earth Energy Imbalance, *J. Clim.* **27**, 3129-3144 (2014).
14. Xie, S. P., Kosaka, Y. & Okumura, Y. M. Distinct energy budgets for anthropogenic and natural changes during global warming hiatus. *Nat. Geosci.* **9**, 29-33 (2016).
15. Piecuch, C. G., & Quinn, K. J. El Niño, La Niña, and the global sea level budget. *Ocean Sci.* **12**, 1165-1177 (2016).
16. Nerem, R. S. et al. Climate-change-driven accelerated sea-level rise detected in the altimeter era. *Proc. Natl. Acad. Sci. USA* **115**, 2022-2025 (2018).
17. Hamlington, B. D. et al. The Dominant Global Modes of Recent Internal Sea Level Variability. *J. Geophys. Res.* **124**, 2750-2768 (2019).

18. Llovel, W. et al. Terrestrial waters and sea level variations on interannual time scale, *Glob. Planet. Change* **75**, 76-82 (2011).
19. Loeb, N. G. et al. Observed changes in top-of-the-atmosphere radiation and upper-ocean heating consistent within uncertainty. *Nat. Geosci.* **5**, 110-113 (2012).
20. Hamlington, B. D. et al. Origin of interannual variability in global mean sea level. *Proc. Natl. Acad. Sci. USA* **117**, 13983-13990 (2020).
21. Watson, C. S. et al. Unabated global mean sea-level rise over the satellite altimeter era. *Nat. Clim. Change* **5**, 565-568 (2015).
22. Lenssen, N. J. L. et al. Improvements in the GISTEMP uncertainty model. *J. Geophys. Res. Atmos.* **124**, 6307-6326 (2019).
23. Hu, X. et al. Decadal evolution of the surface energy budget during the fast warming and global warming hiatus periods in the ERA-interim. *Clim. Dyn.* **52**, 7339-7357 (2019).
24. Huang, N. E. & Wu, Z. A review on Hilbert-Huang transform: Method and its applications to geophysical studies. *Rev. Geophys.* **46** (2008).
25. Wu, Z. & Huang, N. E. Ensemble empirical mode decomposition: a noise-assisted data analysis method. *Adv. Adapt. Data Anal.* **1**, 1-41 (2009).
26. T. Ezer, Sea level rise, spatially uneven and temporally unsteady: Why the U.S. East Coast, the global tide gauge record, and the global altimeter data show different trends. *Geophys. Res. Lett.* **40**, 5439-5444 (2013).

27. Ji, F., Wu, Z., Huang, J. & Chassignet, E. P. Evolution of land surface air temperature trend. *Nat. Clim. Change* **4**, 462-466 (2014).
28. Cha, S. C., Moon, J. H. & Song, Y. T. A Recent Shift Toward an El Niño-Like Ocean State in the Tropical Pacific and the Resumption of Ocean Warming. *Geophys. Res. Lett.* **45**, 11-885 (2018).
29. Scanlon, B. R. et al. Global models underestimate large decadal declining and rising water storage trends relative to GRACE satellite data. *Proc. Natl. Acad. Sci. USA* **115**, E1080-E1089 (2018).
30. Cheng, L., Zheng, F. & Zhu, J. Distinctive ocean interior changes during the recent warming slowdown. *Sci. Rep.* **5**, 1-11 (2015).
31. Durack, P. J., Gleckler, P. J., Landerer, F. W. & Taylor, K. E. Quantifying underestimates of long-term upper-ocean warming. *Nat. Clim. Change* **4**, 999-1005 (2014).
32. Chen, J. L., Wilson, C. R., & Tapley, B. D. The 2009 exceptional Amazon flood and interannual terrestrial water storage change observed by GRACE. *Water Resour. Res.* **46**, W12526 (2010).
33. Aragão, L. E.O.C. et al. 21st Century drought-related fires counteract the decline of Amazon deforestation carbon emissions. *Nat. Commun.* **9**, 1-12 (2018).
34. Tapley, B. D. et al. Contributions of GRACE to understanding climate change. *Nat. Clim. Change* **9**, 358-369 (2019).

35. Mantua, M. J., Hare, S. R. Zhang, Y., Wallace, J. M. & Francis, R. C. A Pacific Interdecadal Climate Oscillation with Impacts on Salmon Production. *Bull. Am. Meteorol. Soc.* **78**, 1069-1080 (1997).
36. Newman, M. et al. The Pacific Decadal Oscillation, Revisited. *J. Clim.* **29**, 4399-4427 (2016).
37. Zhang, Y., He, B., Guo, L. & Liu, D. Differences in Response of Terrestrial Water Storage Components to Precipitation over 168 Global River Basins. *J. Hydrometeorol.* **20**, 1981-1999 (2019)
38. Roemmich, D. et al. Unabated planetary warming and its ocean structure since 2006. *Nat. Clim. Change* **5**, 240-245 (2015).
39. Shepherd, A. et al. Mass balance of the Greenland Ice Sheet from 1992 to 2018. *Nature* **579**, 233-239 (2020).
40. Llovel, W. & Terray, L. Observed southern upper-ocean warming over 2005–2014 and associated mechanisms. *Environ. Res. Lett.* **11**, 124023 (2016).
41. Johnson, G. C. & Birnbaum, A. N. As El Niño builds, Pacific Warm Pool expands, ocean gains more heat. *Geophys. Res. Lett.* **44**, 438-445 (2017).
42. Johnson, G. C. & Lyman, J. M. & Loeb, N. G. Improving estimates of Earth's energy imbalance, *Nat. Clim. Change* **6**, 639-640 (2016).

43. Purkey, S. G. & Johnson, G. C. Warming of Global Abyssal and Deep Southern Ocean Waters between the 1990s and 2000s: Contributions to Global Heat and Sea Level Rise Budgets. *J. Clim.* **23**, 6336-6351 (2010).
44. Hansen, J., Sato, M. & Kharecha, P. Earth's Energy Imbalance and Implications. *Atmos. Chem. Phys.* **11**, 13421-13449 (2011).
45. Levitus, S. et al. World ocean heat content and thermosteric sea level change (0–2000 m), 1955–2010. *Geophys. Res. Lett.* **39**, L10603 (2012).
46. Fu, L.-L. On the Decadal Trend of Global Mean Sea Level and Its Implication on Ocean Heat Content Change. *Front. Mar. Sci.* **3**, 37 (2016).
47. Meyssignac, B. et al. Measuring Global Ocean Heat Content to Estimate the Earth Energy Imbalance. *Front. Mar. Sci.* **6**, 432 (2019).
48. Trenberth, K. E. & Fasullo, J. T. Tracking Earth's Energy. *Science* **328**, 316-317 (2010).
49. Johnson, G. C., Lyman, J. M. & Purkey, S. G. Informing Deep Argo Array Design Using Argo and Full-Depth Hydrographic Section Data. *J. Atmos. Oceanic Technol.* **32**, 2187-2198 (2015).

## Methods References

50. Peltier, W. R. Global glacial isostasy and the surface of the ice-age Earth: the ICE-5G (VM2) model and GRACE. *Annu. Rev. Earth Planet. Sci.* **32**, 111-149 (2004).
51. Beckley, B. D., Callahan, P. S., Hancock III, D. W., Mitchum, G. T. & Ray, R. D. On the “Cal-Mode” Correction to TOPEX Satellite Altimetry and Its Effect on the Global Mean Sea Level Time Series. *J. Geophys. Res. Oceans* **122**, 8371-8384 (2017).
52. Ishii, M. & Kimoto, M. Reevaluation of historical ocean heat content variations with time-varying XBT and MBT depth bias corrections. *J. Oceanogr.* **65**, 287-299 (2009).
53. Good, S. A., Martin, M. J. & Rayner, N. A. EN4: Quality controlled ocean temperature and salinity profiles and monthly objective analyses with uncertainty estimates. *J. Geophys. Res. Oceans* **118**, 6704-6716 (2013).
54. Chambers, D. P. et al. Evaluation of the Global Mean Sea Level Budget between 1993 and 2014. *Surv. Geophys.* **38**, 309-327 (2017).
55. Von Schuckmann, K. & Le Traon, P. Y. How well can we derive Global Ocean Indicators from Argo data?. *Ocean Sci.* **7**, 783-791 (2011).
56. A. Shepherd et al. A reconciled estimate of ice-sheet mass balance. *Science* **338**, 1183-1189 (2012).
57. Zemp, M. et al. Global glacier mass changes and their contributions to sea-level rise from 1961 to 2016. *Nature* **568**, 382-386 (2019).

58. Marzeion, B., Leclercq, P. W., Cogley, J. G. & Jarosch, A. H. Brief Communication: Global reconstructions of glacier mass change during the 20th century are consistent. *Cryosphere* **9**, 2399-2404 (2015).
59. Leclercq, P. W., Oerlemans, J. & Cogley, J. G. Estimating the glacier contribution to sea-level rise for the period 1800–2005. *Surv. Geophys.* **32**, 519 (2011).
60. Cogley, J. G. Geodetic and direct mass-balance measurements: comparison and joint analysis. *Ann. Glaciol.* **50**, 96-100 (2009).
61. Wiese, D. N., Landerer, F. W. & Watkins, M. M. Quantifying and reducing leakage errors in the JPL RL05M GRACE mascon solution. *Water Resour. Res.* **52**, 7490-7502 (2016).
62. Peltier, W. R., Argus, D. F. & Drummond, R. Comment on “An Assessment of the ICE-6G\_C (VM5a) Glacial Isostatic Adjustment Model” by Purcell et al. *J. of Geophys. Res. Solid Earth* **123**, 2019-2028 (2018).
63. Wouters, B., Gardner, A. S. & Moholdt, G. Global glacier mass loss during the GRACE satellite mission (2002-2016). *Front. Earth Sci.* **7**, 96 (2019).
64. Groh, A. et al. Evaluating GRACE Mass Change Time Series for the Antarctic and Greenland Ice Sheet—Methods and Results. *Geosciences* **9**, 415 (2019).
65. Reichle, R. H. et al. Assessment and enhancement of MERRA land surface hydrology estimates. *J. Clim.* **24**, 6322-6338 (2011).

66. Reichle, R. H. et al. Assessment of MERRA-2 land surface hydrology estimates. *J. Clim.* **30**, 2937-2960 (2017).
67. Lyman, J. M. et al. Robust warming of the global upper ocean. *Nature* **465**, 334-337 (2010).
68. Huang, N. E. et al. The empirical mode decomposition and the Hilbert spectrum for nonlinear and non-stationary time series analysis. *Proc. R. Soc. Lond. A* **454**, 903-995 (1998).
69. Meehl, G. A., Hu, A. & Teng, H. Initialized decadal prediction for transition to positive phase of the Interdecadal Pacific Oscillation. *Nat. Commun.* **7**, 1-7 (2016).
70. Mudelsee, M. *Climate time series analysis: classical statistical and bootstrap methods*. Vol. 42, 474 (Springer, 2010).
71. Chen, X., Feng, Y. & Huang, N. E. Global sea level trend during 1993-2012. *Glob. Planet Change* **112**, 26-32 (2014).

# Figures

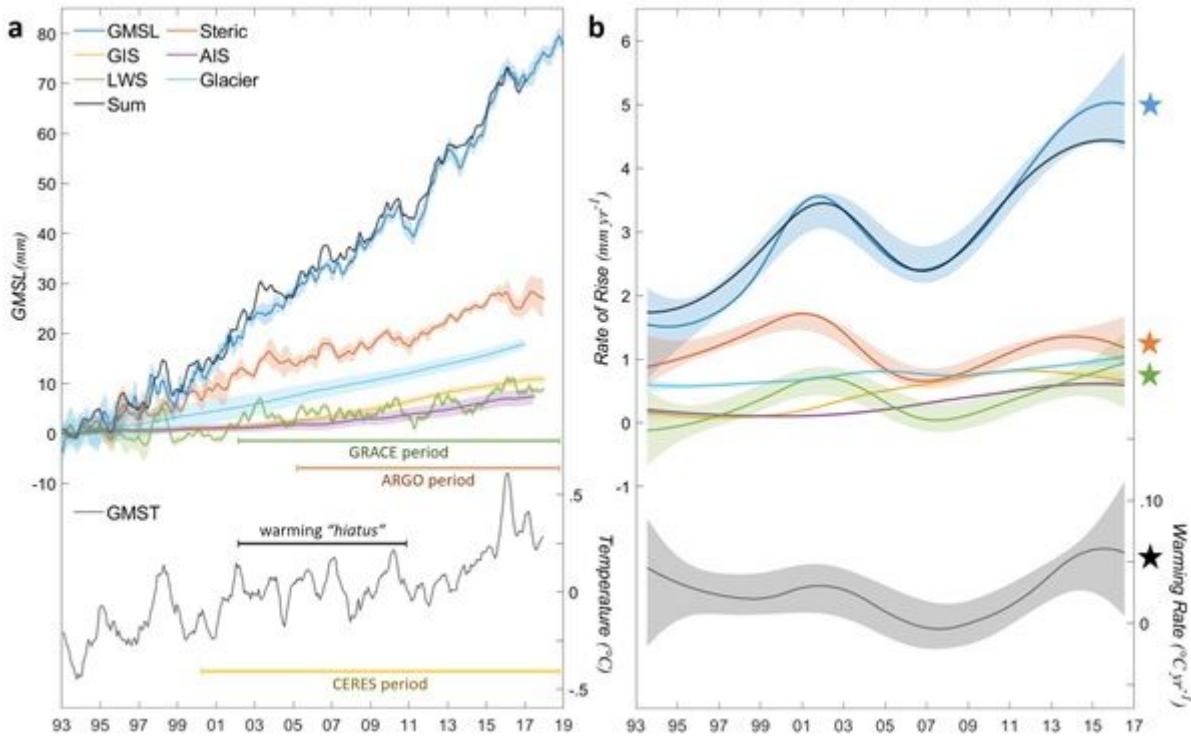


**Figure 1**

GMSL budget and GMST. (a) Time series of all sea-level components (upper) and GMST (bottom), including the ensemble mean GMSL using altimetry data from six processing groups (blue, see Materials and Methods), sum of ensemble mean components (black), individual ensemble mean components, and GMST using the Goddard Institute for Space Studies Surface Temperature Analysis v422. Uncertainties are based on the dispersion among different time series around the mean (coloured shades). (b) Instantaneous rate of GMSL trend with decadal variability (upper) and GMST trend (bottom) from EEMD analysis. A bootstrap method based on random resampling to estimate confidence intervals (coloured shades) was used to test the significance (see Materials and Methods). Time series with decadal shift are highlighted (star symbols).

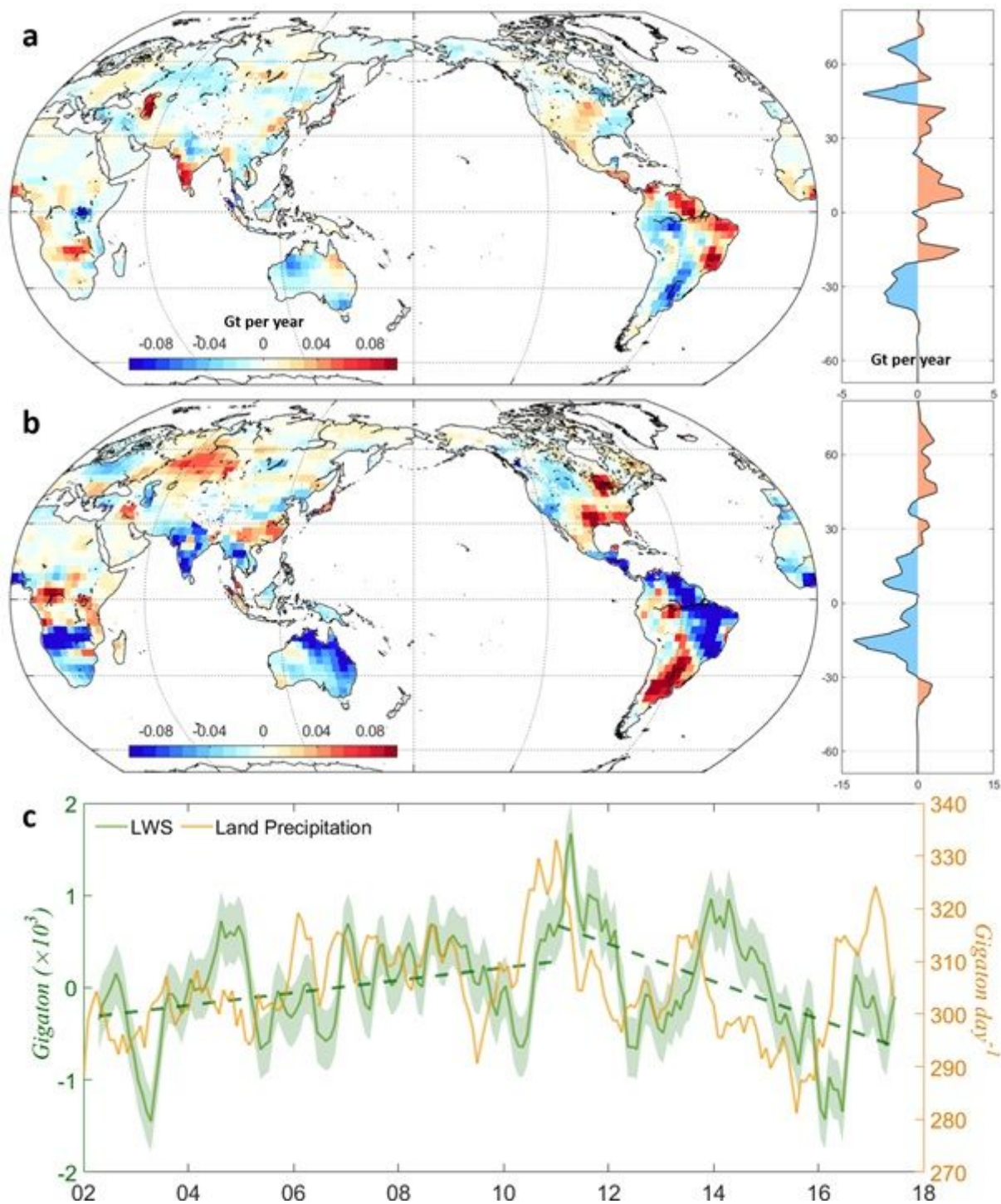


**Figure 2**

Trends in LWS from GRACE observations. Global map of LWS trend and its zonal total trend in (a) in 2002–2010 and (b) 2011–2017. (c) Time series of global LWS (green) from GRACE and land precipitation (yellow) from GPCP. The linear trend throughout the GRACE period was removed to highlight climate-driven decadal trend shift in LWS. The dashed lines indicate the linear trends in 2002–2010 and 2011–2017. The LWS uncertainties are shown in coloured shades (see Materials and Methods). Note: The designations employed and the presentation of the material on this map do not imply the expression of any opinion whatsoever on the part of Research Square concerning the legal status of any country,

territory, city or area or of its authorities, or concerning the delimitation of its frontiers or boundaries. This map has been provided by the authors.

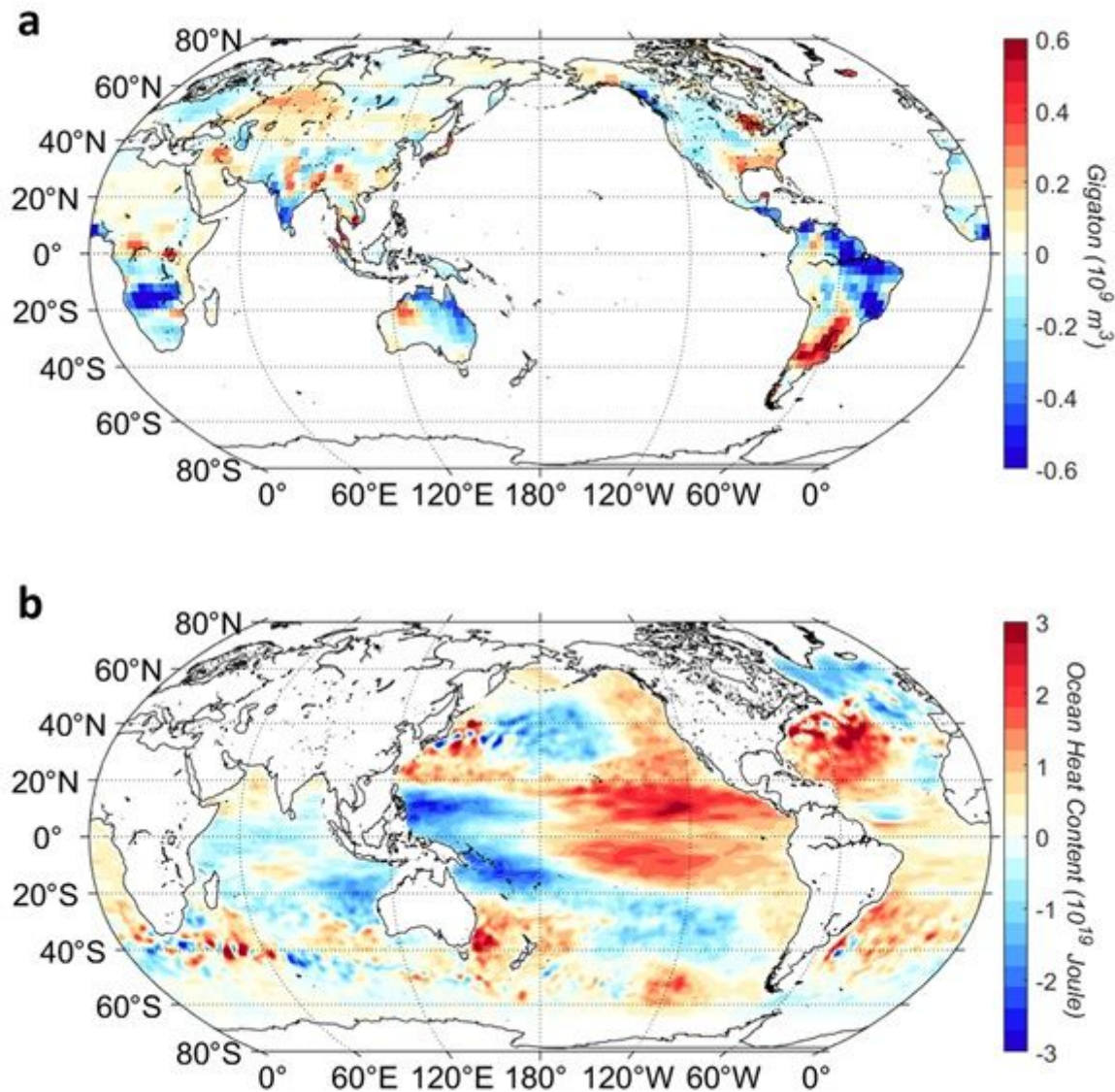


**Figure 3**

Global LWS and OHC fingerprints with respect to the PDO. (a, b) LWS and OHC (0-2000 m) regressed onto the decadal mode of the PDO (shown in Supplementary Fig. 5c) over 2002–2017 and 2005–2017, respectively. Data sources are GRACE mascon solution (JPL RL06Mv2) for LWS and SCRIPPS for OHC, respectively. Note: The designations employed and the presentation of the material on this map do not imply the expression of any opinion whatsoever on the part of Research Square concerning the legal status of any country, territory, city or area or of its authorities, or concerning the delimitation of its frontiers or boundaries. This map has been provided by the authors.

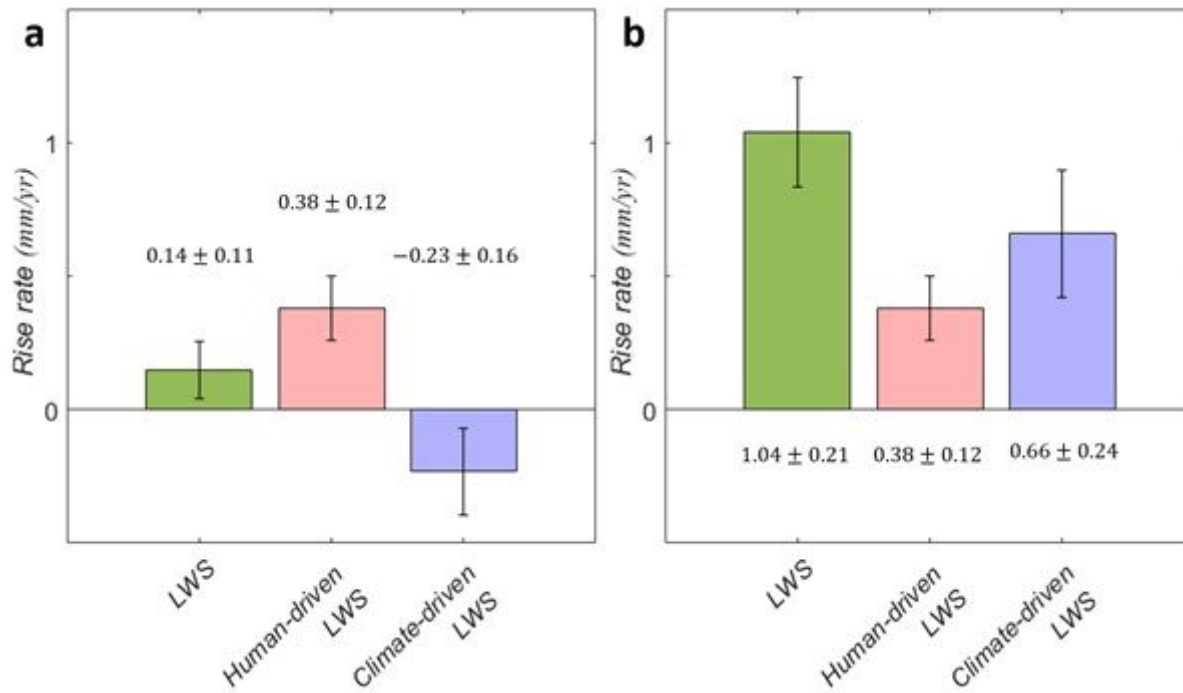


**Figure 4**

Disaggregation of net LWS terms. (a) 2002–2010. (b) 2011–2017. Left bar: Glacier-free LWS, middle bar: human-driven LWS estimated by IPCC AR 51, and right bar: Climate-driven LWS (i.e. subtracting the IPCC estimate for human-driven change). Error bars represent 95% confidence intervals estimated from slope of uncertainty and the quadratic sum.

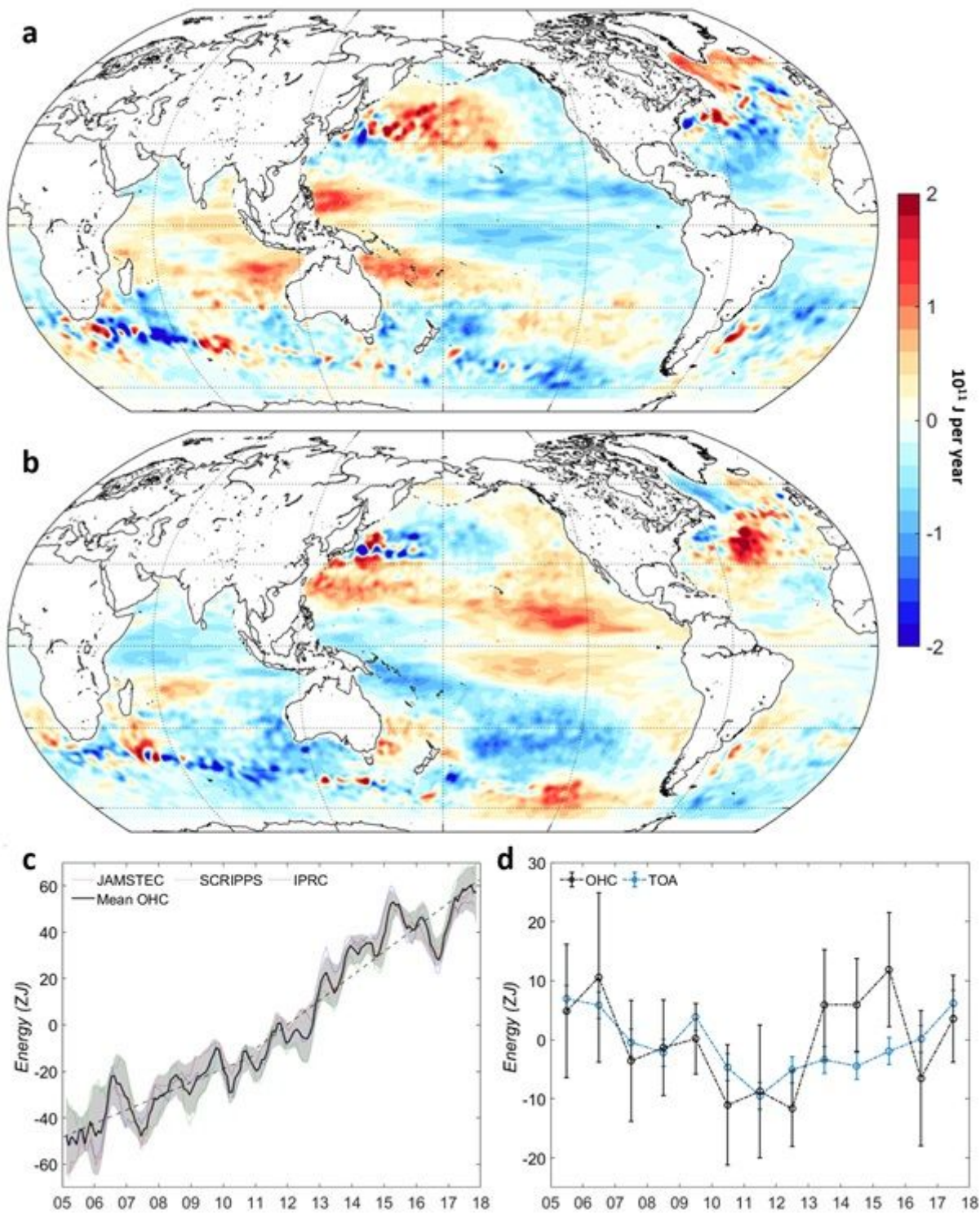


**Figure 5**

Argo-derived OHC trends and TOA net energy storage. Global map of upper-2000 m OHC trend from the SCRIPPS data during (a) 2005–2010 and (b) 2011–2017. (c) Ensemble mean of globally integrated OHC (black) based on three Argo products (see Materials and Methods) and their individual values (coloured lines). The shaded areas denote one standard deviation around the mean. (d) Comparison between the yearly OHC (black) and TOA net energy storage (blue). Each component was detrended for the study period. The OHC uncertainties (black bar) are shown at one standard error of the mean, and TOA annual

random errors (blue bar) are based on Johnson41. Note: The designations employed and the presentation of the material on this map do not imply the expression of any opinion whatsoever on the part of Research Square concerning the legal status of any country, territory, city or area or of its authorities, or concerning the delimitation of its frontiers or boundaries. This map has been provided by the authors.

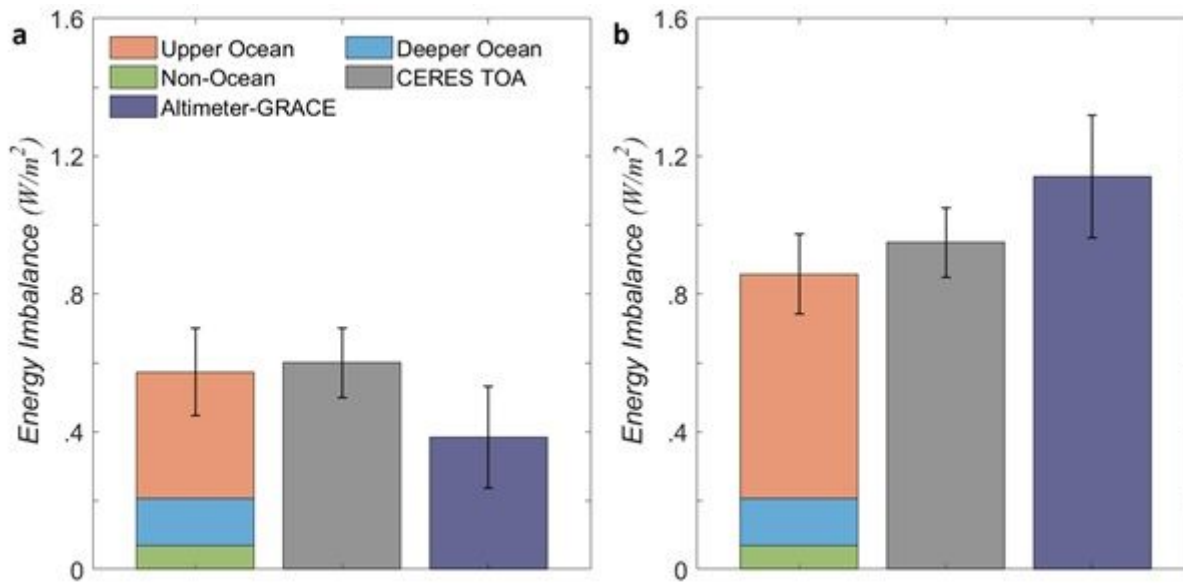


**Figure 6**

Three independent estimated contribution to EEI. (a) 2005–2010. (b) 2011–2017. Left bar: in situ observational estimate of ocean heat uptake by combining Argo-based upper ocean (0–2000 m) and previously published estimates of heat uptake by the deeper ocean terms<sup>42</sup> and non-ocean term<sup>43</sup>; middle: direct CERES satellite measurements of TOA net energy flux, and right: altimetry minus GRACE residual approach. Error bars represent 95% confidence intervals estimated from slopes of uncertainty fitted to each data. Uncertainties of CERES TOA flux are shown at one standard deviation ( $0.1 W m^{-2}$ ) based on Johnson<sup>41</sup>.

## Supplementary Files

This is a list of supplementary files associated with this preprint. Click to download.

- [SupplementaryInformation.docx](#)